Carbon Aerogel-Supported Iron for Gasification Gas Cleaning: Tars Decomposition

Oscar Gómez-Cápiro [1,2,3,*], Kimberley Matschuk [3], Tim Schulzke [3], Romel Jiménez Concepción [1] and Luis E. Arteaga-Pérez [2,4,*]

[1]   Carbon and Catalysis Laboratory (CarboCat), Department of Chemical Engineering, Faculty of Engineering, University of Concepción, Concepción 403000, Chile; romeljimenez@udec.cl

[2]   Unidad de Desarrollo Tecnológico, University of Concepción, Concepción 4191996, Chile

[3]   Fraunhofer UMSICHT, Institute for Environmental, Safety, and Energy Technology, 46047 Oberhausen, Germany; kimberley.matschuk@umsicht.fraunhofer.de (K.M.); tim.schulzke@umsicht.fraunhofer.de (T.S.)

[4]   Laboratory of Thermal and Catalytic Processes (LPTC-UBB), Wood Engineering Department, Faculty of Engineering, University of Bío-Bío, Concepción 4030000, Chile

[*]   Correspondence: oscar.gomez-capiro@cec.mpg.de (O.G.-C.); larteaga@ubiobio.cl (L.E.A.-P.)

Abstract: Tar removal from gasification gases is a determinant step to guarantee the operational feasibility of gasification-to-chemicals/energy systems. However, this is a very complex process requiring catalytic materials to proceed under reasonably low temperatures and to convert the tars into fuel gases (i.e., CH_x). The use of Fe-based catalysts for application has been reported before, however, there are still unsolved questions related to its stability and interaction with some species of gasification gases. Therefore, we evaluated carbon-supported Fe for the decomposition of tar using simulated gasification gases, and toluene, naphthalene, and benzene as models for tar. The effects of temperature ($565 < T < 665\ ^\circ C$) and co-feeding CO on the catalytic activity and stability were inspected at laboratory and bench scales. The activity of catalysts for decomposing tars was in the following order: benzene > toluene e > naphthalene. Moreover, there was evidence validating a reversible elemental step toluene⇌benzene over the Fe surface. The characterization of the spent catalysts evidenced the oxidation of the active phase and the carbon deposition on the surface. The formation of Fe_xO_y caused a marked loss of activity. Conversely, the carbides were stable and still active for tar decomposition.

Keywords: gasification; tars; catalytic conversion

1. Introduction

Gasification is one of the most promising processes to produce energy from biomass [1]. The tuning of gasifier operation conditions allows the production of a syngas-like product with several applications [2]. However, regardless of the biomass source, reactor model or operational conditions, the gasification gas contains tars. The tarry fraction of the syngas is detrimental to most technologies using gasification gases as feedstock, even for small concentrations (in the order of ppm). Therefore, the elimination, removal, or conversion of tar into valuable products, are among the main concerns in the endeavor to establish the biomass-to-energy/chemicals route via gasification [3]. The literature reports several ways to remove tar, most requiring post-treatments to guarantee target concentrations [4]. Several authors ascribe the major challenges for transforming tars into simpler molecules to their complex and reactive chemical composition. In this sense, thermal and catalytic cracking are attractive processes to break down the poly-(mono)aromatic structure of tars into valuable gases. However, the results obtained to date are still far from commercial application [5–7]. In the case of the catalytic processes, there is a lack of information on the reaction mechanisms describing catalytic tar conversion, thus an insufficient development

of active and stable catalysts. Meanwhile, the thermal (non-catalytic) decomposition of tar exhibits low conversion for mono and poly-aromatics at temperatures close to the gasification process; a high energy consumption is required to achieve the required conversions [8,9].

For the conversion of catalytic tar, metallic active sites play a relevant role in achieving the primary tar cracking and the further radicals–ring bonds and C–H bonds scissions (only in molecules with radicals as methyl in toluene) at reasonable temperature levels, viz., close to gasification gases [10].

Among the most common catalysts for gasification gas cleaning, olivines and dolomites stand out as natural solids easy to handle and dispose [11–13]. However, dolomites are highly sensitive to chlorine poisoning and suffer erosion and deactivation at high temperatures, while olivines have lower activity but a higher resistance to erosion [14]. A common issue of these catalysts is coke deposition, which leads to the rapid blockage of pores, reducing catalytic activity [15]. Recently, supported transition metals (mainly Fe and Ni) have emerged as candidates for the catalytic upgrading of gasification gas [13,16]. Nickel catalysts have shown high selectivity to H_2 [17] and a lower apparent activation energy for tar decomposition than other transition metals [18]. During pine sawdust gasification, the use of Ni catalysts led to an improvement of fuel gas production; but the catalyst was prone to sintering [19]. Other studies reported an increment in H_2 and CO yields while CO_2 decreased when using $Ni/\gamma\text{-}Al_2O_3$ catalyst with metal loading between 4% and 8% wt [20]. The activity of this metal as an active phase for tar decomposition was mainly affected by coke deposition and sulfur poisoning [21].

Iron is the most active metal for breaking C–C bonds, and it is also more environmentally friendly and economically accessible than other transition metals [13,22,23]. Moreover, Fe is the main active phase to produce light hydrocarbons via gasification and tar conversion (up to 96% has been reported using Fe supported as catalyst) [13]. Alumina-supported Fe catalyst (10% wt of metal) was tested in toluene decomposition, reaching 57% conversion at 750 °C and obtaining benzene as one of the main products [24]. Other authors tested the activity of Fe oxides supported on silicalite-1 (15% wt of metal) for toluene decomposition; the conversion at 700 °C was 34.8%, which suggested that Fe oxides were active for tar decomposition [25]. Madadkhani et al. [26] demonstrated the flexibility of Fe for this application, by applying bauxite residues to produce a catalyst capable of converting up to 98% of naphthalene (model tar). However, similar to Ni, Fe is deactivated during gasification gas treatment, owing to Fe^0 oxidation, coke deposition, poisoning, or sintering [27]. An example is the same study of Madadkhani et al., which reported a reduction of 33% in the tar conversion after 14 h of operation [26]. This reduction in activity can be mitigated by controlling operational parameters (injecting air, steam) or from the design of the catalyst. In the latter, the selection of the support has a strong influence, mainly by using supports resistant to coke deposition. Among other factors, this resistance can be tailored by changing the acidity and the solid's crystalline structure, or by providing a sufficient surface to obtain a high dispersion of the metal clusters on the support [28].

In particular, carbonaceous supports have attracted attention because of their controllable properties and renewability [29]. The textural properties (surface area and pore size distribution), surface chemical composition, and redox capacity are among the crucial aspects in carbons. Moreover, carbon supports could have intrinsic activity for tar conversion, as was demonstrated by [30], who obtained high yields of benzene as a product from toluene pyrolysis, by using activated carbon as a catalyst. Similar results were reported by Fuentes-Cano et al., after testing three chars to decompose toluene or naphthalene [31]. Among carbon-based supports, carbon aerogels (CAG) have shown exceptional properties as adsorbents and catalyst supports [32–34]. CAG have previously been used as Fe support for upgrading pyrolysis vapors, reaching 70% conversion of carboxylic acids, while increasing the selectivity of hydrogenation [35,36].

Despite the plethora of works published in this field, the relationship between catalyst properties and operational parameters, with the reaction mechanisms of tar decomposition,

remains unsolved [37]. Mukai et al., performed in situ kinetic measurements to study the conversion of aromatics and aliphatic compounds (as tar models) over Ni/LSAO and Ni/αAl$_2$O$_3$, and concluded that the nature of the support had a strong influence on the reaction mechanism (e.g., providing oxygen or adsorbing tar compound) [38]. Kaisalo et al., also studied the kinetics of benzene reforming over Ni/Al$_2$O$_3$, accurately fitting the experimental data to a first order kinetic model [39]. However, the limited capability of the first-order with respect to tar concentration for describing the reaction mechanism appears as a limitation of these valuable analyses. Moreover, there are no reports proposing plausible reaction mechanisms for the conversion of tar (toluene, naphthalene, and benzene as models) over CAG-supported Fe catalysts.

Therefore, the present work aims to understand the mechanism for tar decomposition over CAG-supported Fe catalysts by studying the effect of temperature and the role of some gasification gases (CO). Moreover, the influence of the metal oxidation state and coke deposition on the reaction performance is also posed as a question in our analysis.

2. Results

2.1. Compositional Analysis of Support

The support contained 91.2% wt of elemental carbon, which is characteristic of carbon aerogels (CAG) according to Standard 472:1999. Nitrogen, hydrogen and oxygen were 1.7%, 0.8% and 5.3% wt, respectively. The inductively coupled plasma optical emission spectroscopy (ICP-OES) analysis did not evidence any inorganic element in a concentration capable of causing a significant change in the catalytic activity.

2.2. CAG Surface Characterization

Figure 1a–c shows the N$_2$ adsorption–desorption isotherms for CAG, Fe/CAG, and Fe/CAG-ps. The specific surface (by BET model) and the average pore size obtained for the support were 370 m^2/g and 11 nm, respectively. Normally, after active phase impregnation, CAG lose part of their specific surface, which was confirmed here for Fe/CAG (249 m^2/g) and Fe/CAG-ps (304 m^2/g). The shape of the isotherm and the hysteresis loops found are quite common for biochars. Previous reports ascribed these results to restricted diffusion of N$_2$ or irreversible pore deformation by the sorbate. Liquid displacement and sedimentation measurements cause swelling, that is, the internal matrix expands in response to the presence of N$_2$ [40]. The presence of metals alters the CAG pore morphology, as evidenced here by the behavior of the hysteresis, classified as type H4 for the catalysts, which are typical for zeolites and micro-mesoporous carbons [41]. Based on these results, it was confirmed that the catalysts and the support had favorable textural properties for tar diffusion. In particular, they had sufficient specific surface area for the active phase to be adequately dispersed, and the average pore sizes were of suitable dimensions for diffusion of the model tar molecules used here (the largest being naphthalene, at approximately 0.72 nm).
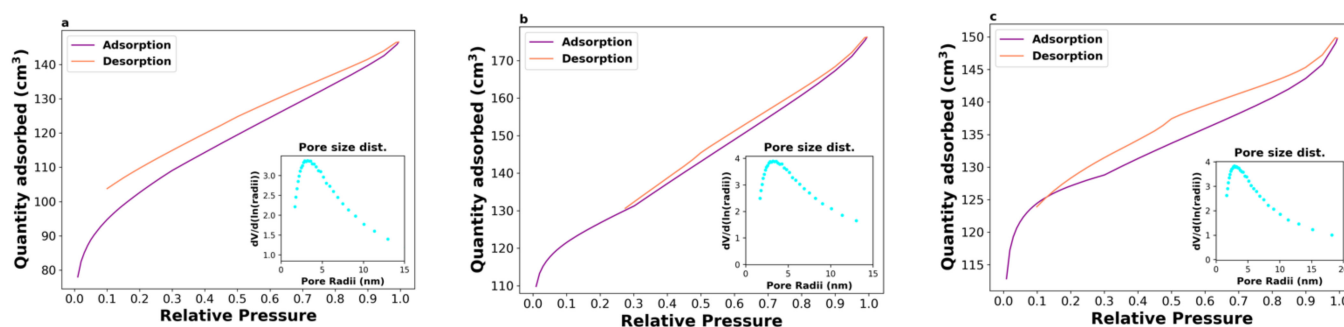
Figure 1. N$_2$ adsorption–desorption isotherms at 77 K and pore size distribution on: (**a**) CAG, (**b**) Fe/CAG, and (**c**) Fe/CAG-ps.

2.3. Particle Size Distribution and Metallic Surface

The reactions implying the break of C–C bonds are sensitive to the metal particle structure and the presence of edges, more common on particle sizes lower than 10 nm [42]. Above this size, the surface is determined by the termination of the bulk structure, as in the case of the catalysts prepared here [43]. The average particle sizes calculated from transmission electron microscopic images (TEM) were 22.2 ± 0.73 nm for Fe/CAG and 11.9 ± 0.21 nm for Fe/CAG-ps (Figure 2a,b). According to the ICP-OES, Fe/CAG had 10.5% wt, and Fe/CAG-ps 7.4% wt, of metal, respectively. This implied that Fe dispersion on Fe/CAG and Fe/CAG-ps surfaces were 6.6% and 9.2%, respectively. Finally, exposed Fe (moles of metal in cluster surface/grams of metal impregnated) were estimated from these results to calculate turn over frequency (TOF) values (Figure 2c,d).
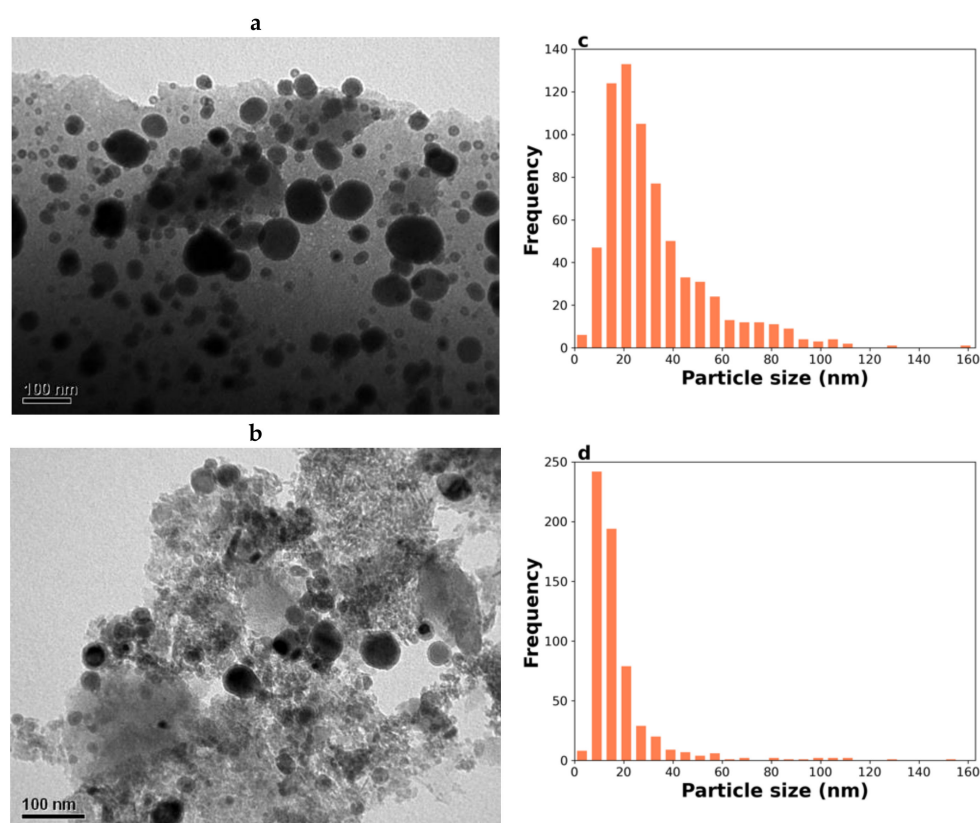
Figure 2. Transmission electron microscopy image and particle size distribution (PZD) of the catalysts: (**a**) Fe/CAG image, (**b**) Fe/CAG-ps image, (**c**) Fe/CAG PZD, and (**d**) Fe/CAG-ps PZD.

The slight difference between the dispersion measured for Fe/CAG and Fe/CAG-ps was attributed to the thermal response of the pellets during the reduction. In this case, the heat transfer limitation to the pellet interior led to a milder reduction, thus to lower cluster sizes. However, regardless of the shape of the catalysts, both dispersions were lower than 10%, which allowed us to rule out the effect of surface coordination on the catalytic activity for tar decomposition. In other words, any difference observed in the catalytic activity could be attributed only to the nature of the active phase.

2.4. Throughput Study on Tar Decomposition over Fe/CAG

2.4.1. Kinetic Measurements

The effect of external mass transport limitations on the kinetic data gathered for toluene decomposition over Fe/CAG were excluded by applying the Mears criterion, which resulted in the effect being far below the established limit ($2.06 \times 10^{-9} < 0.15$). Additionally,
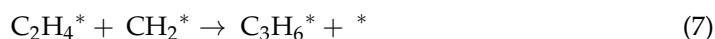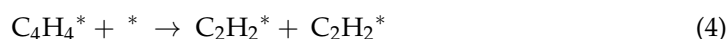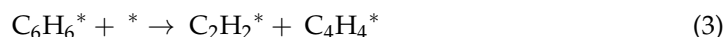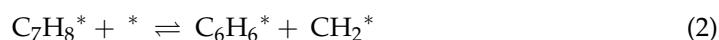
the internal mass transfer limitations were excluded by using the Weizs–Prater criteria ($1.78 \times 10^{-3} < 0.3$) [44].

Figure 3a shows an example of an experiment at 600 °C and 1979 ppm of toluene decomposition. It was observed that benzene (primary product) concentration spiked to 8.9×10^{-6} mol/s as toluene was converted during the first 2 h. From this point, benzene started converting, while toluene flow increased to plateau at 2.2×10^{-7} mol/s. This result suggested that toluene and benzene were involved in a reversible step. This reversibility was studied by adding benzene to the feed and the results are shown in Figure 3b. Given that pure benzene was injected, detecting toluene during the first 4 h of the experiment demonstrated that a quasi-equilibrated reversible step, as represented in Equation (2), was taking place. In this case, the reaction mechanism started with benzene adsorption (Equation (1)), and the *CH_2 radicals formed after the ring breaking (Equations (3) and (4)) may have reacted with other adsorbed benzene molecules to form toluene again (Equation (2)). Toluene was no longer detectable 5 h after the start of the test and a quasi-steady state was reached, with propylene being the main species detected in the gas stream.
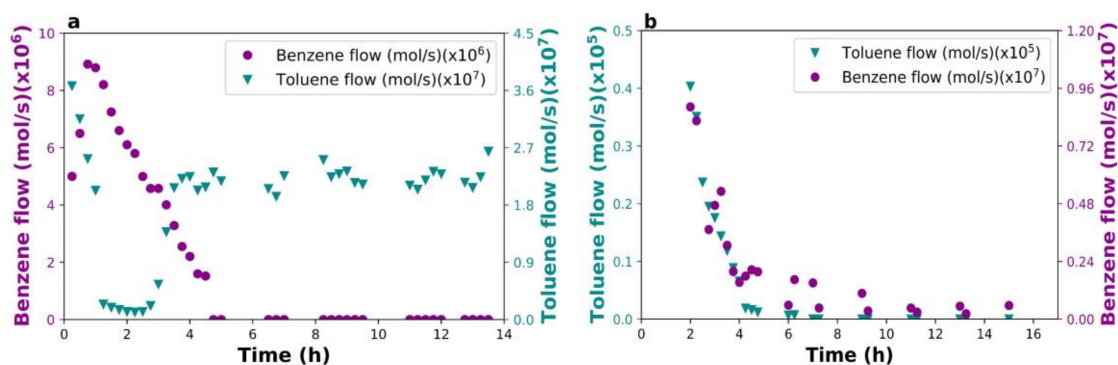
Figure 3. Tar model decomposition: (**a**) toluene (1979 ppm) decomposition over Fe/CAG catalyst, (**b**) benzene (1175 ppm) decomposition over Fe/CAG catalyst; temperature, 600 °C; space velocity, 350 mL/(min·g_{cat}).

The following elementary steps imply that the aromatic rings break into segments formed by two carbon atoms as proposed by Oemar et al. [45], which, according to Equation (3), takes place on two active Fe sites. Without any oxidizing or reducing agents to remove carbon atoms, the subsequent steps imply carbon deposition (Equation (5); confirmed here by SEM–EDX analysis, Table 1). Intermediate CH_2 * promotes the propagation of the aliphatic chain and the formation of ethylene and propylene as described by elementary steps Equations (6) and (7).

$$C_7H_8 + {}^* \rightleftharpoons C_7H_8{}^* \tag{1}$$

$$C_7H_8{}^* + {}^* \rightleftharpoons C_6H_6{}^* + CH_2{}^* \tag{2}$$

$$C_6H_6{}^* + {}^* \rightarrow C_2H_2{}^* + C_4H_4{}^* \tag{3}$$

$$C_4H_4{}^* + {}^* \rightarrow C_2H_2{}^* + C_2H_2{}^* \tag{4}$$

$$C_2H_2{}^* + {}^* \rightarrow CH_2{}^* + C^* \tag{5}$$

$$2\,CH_2{}^* \rightarrow C_2H_4{}^* + {}^* \tag{6}$$

$$C_2H_4{}^* + CH_2{}^* \rightarrow C_3H_6{}^* + {}^* \tag{7}$$

$$C_6H_6{}^* \rightleftharpoons C_6H_6 + {}^* \tag{8}$$

$$C_3H_6{}^* \rightleftharpoons C_3H_6 + {}^* \tag{9}$$

$$C^* \rightarrow C + {}^* \tag{10}$$

Table 1. C/Fe ratio of spent catalysts at different toluene concentrations in the inlet. Elements detected by electron microscopy–energy dispersive X-ray spectroscopy (SEM–EDX). The space velocity of the experiments was 700 mL/(min g$_{cat}$) except when another value is specified.

Catalyst	C/Fe Ratio
Fe/CAG 575–990 ppm	7.14
Fe/CAG 600–990 ppm	5.13
Fe/CAG 625–990 ppm	5.58
Fe/CAG 575–990 ppm SV 875	6.84
Fe/CAG 600–990 ppm SV 875	6.72
Fe/CAG 625–990 ppm SV 875	7.22
Fe/CAG 625–1485 ppm	5.97
Fe/CAG 625–1979 ppm	8.71

A simplified model based on Langmuir–Hinshelwood formalism is proposed to describe the kinetics of the process, including the effects of reactant and intermediate interaction on the surface (Equation (11)):

$$\text{TOF} = \frac{k_3 K_1 K_2 p_{toluene}}{\left(1 + \sum K_i p_i\right)^2} \tag{11}$$

where k_3 is the forward kinetic constant for the third step (Equation (3)); K_1 is the equilibrium constant in the toluene adsorption (Equation (1)); K_2 is the equilibrium constant for the dissociation of adsorbed toluene into benzene and CH_2 * (Equation (2)); $p_{toluene}$ is the toluene partial pressure in the feed; K_i is the adsorption constant related to each reaction intermediate on catalyst surface; and p_i is their corresponding partial pressure.

According to the proposed model, Equation (12) can express the apparent activation energy (E_{app}) as a relation between the activation energy of the RDS and the heat of adsorption for reactant and intermediates.

$$E_{app} = E_3 - Q_{toluene} - Q_2 + Q_i \tag{12}$$

where E_3 is the activation energy of the rate-determining step (RDS), in this case, Equation (3); $Q_{toluene}$ is the adsorption heat corresponding to toluene adsorption, in this case, Equation (1); Q_2 is the heat associated with the equilibrated toluene dissociation; and Q_i represents the adsorption heat of all reaction intermediates on the catalyst surface.

This equation is applied in the upcoming sections to estimate the kinetic parameters describing toluene decomposition on Fe/CAG.

Figure 4 shows the Arrhenius plot where a slope change is evident, which is typical of experiments influenced by mass transfer. However, the mass transfer limitations were discarded, as explained above. Therefore, this kinetic effect can be explained by Equation (12), which suggests that the surface coverage of intermediates is lower at higher temperatures, leading to a reduction in their heat of adsorption, Q_i. The adsorption and dissociation heats of toluene ($Q_{toluene}$ and Q_2) may have higher modular values than the activation energy of the rate-determining step (Equation (11)); this fact, combined with a decrease in Q_i, causes the apparent activation energy (E_{app}) to be negative, and thus the slope of the Arrhenius plot to be negative. If this is the case, the combined effect of higher temperature and lower toluene concentration in the feed must cause a stronger fall in the coverage of intermediates, and a steeper drop in the slope, as evidenced when the lowest concentration of toluene (990 ppm) is fed.

The change in the slopes of Arrhenius plots for different values of toluene concentration in the feed reinforce the previously posed hypothesis of the correlation between surface coverage and the consequent reduction in Q_i. Another explanation might be that at higher temperatures and lower toluene inlet concentrations, the adsorption step became slower and so, consequently, did the RDS. In fact, an RDS resulting in a negative activation energy is commonly associated with exothermic equilibrium reactions—such as the adsorption

step—thus the behavior shown in Figure 4 can be also explained by a change of this nature in the reaction pathways.
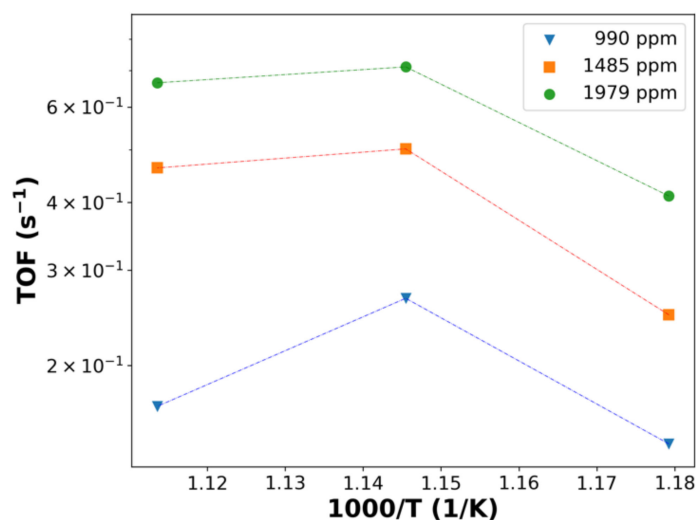

Figure 4. Arrhenius plot for toluene decomposition. Temperature values were 575 °C, 600 °C, and 625 °C. The space velocity was 700 mL/(min·g_{cat}). Catalyst mass of 0.1 g. Note that the y-axis is logarithmic. For TOF calculation the metal exposed surface was as follows: Fe/CAG had 0.03894 mmol Fe/g of the catalyst; Fe/CAG-ps had 0.03789 mmol Fe_s/g of the catalyst.

On the other hand, steps Equations (1) and (6) in the proposed mechanism fail to explain the reduction in TOF represented in Figure 4, thus it can be assumed that C atoms and traces of aromatic rings remain on the catalyst surface, which contribute to C deposition via polymerization reactions. This last point was witnessed by Korus et. al. who detected the formation of polyaromatics from toluene under similar temperatures as those used here [30].

Post-reaction characterization of the catalysts using X-ray diffraction (XRD) was made to verify changes in the crystalline phases during the reaction. It is well known that the iron metallic phase is active for C–C bond breaking, but the oxide phase has a lower activity [23]. The XRD patterns (Figure 5) of spent catalysts show oxidized Fe phases (Table A1), which suggest that the decreases observed in the catalytic activity were due to Fe oxidation. According to these results, and considering that O_2 was not fed into the reactor, the Fe oxidation is ascribed to the formation of metal-support complexes in the absence of H_2. Therefore, it can be inferred that no H_2 was formed from toluene decomposition, which supports its exclusion from the mechanism as previously proposed. In addition, there were no significant differences in crystallite sizes of Fe and oxides clusters, suggesting that metal sintering may play a role in deactivation (Table A2).

Figure 6 shows the percentages of the XRD peak areas corresponding to metallic Fe, which were calculated as the ratio of Fe^0 peaks area/total pattern area; it was observed that the amount of active phase (metallic Fe) rose with temperature, while the space velocity showed a lower effect on Fe^0 concentration. These results also allowed the discard of sintering and oxidation as the main deactivation causes at higher temperatures. It is important to note that the $FeO:Fe_3O_4$ ratio was almost constant at 3:2, and independent of the reaction conditions, which indicated that the type of iron oxide had no influence on the activity loss.

The C/Fe ratios of the spent catalysts demonstrated that the amount of carbon increased at higher temperatures regardless of the toluene concentration fed and space velocity used (Table 1). This can only be explained by the formation of polyaromatics (PAHs) and coke deposition.
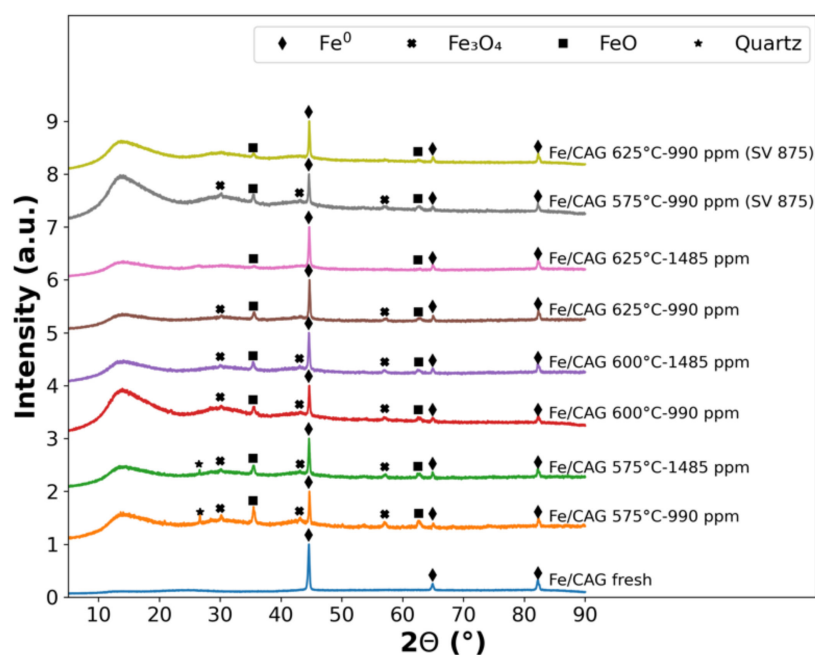
Figure 5. Normalized XRD patterns of fresh and spent catalysts during toluene decomposition. Each pattern is identified with the corresponding spent catalyst condition, temperature, and toluene concentration in the feed. All experiments were carried out at 700 mL/(min·g_{cat}), except for the spent catalyst marked SV 875, which was performed at 875 mL/(min·g_{cat}).
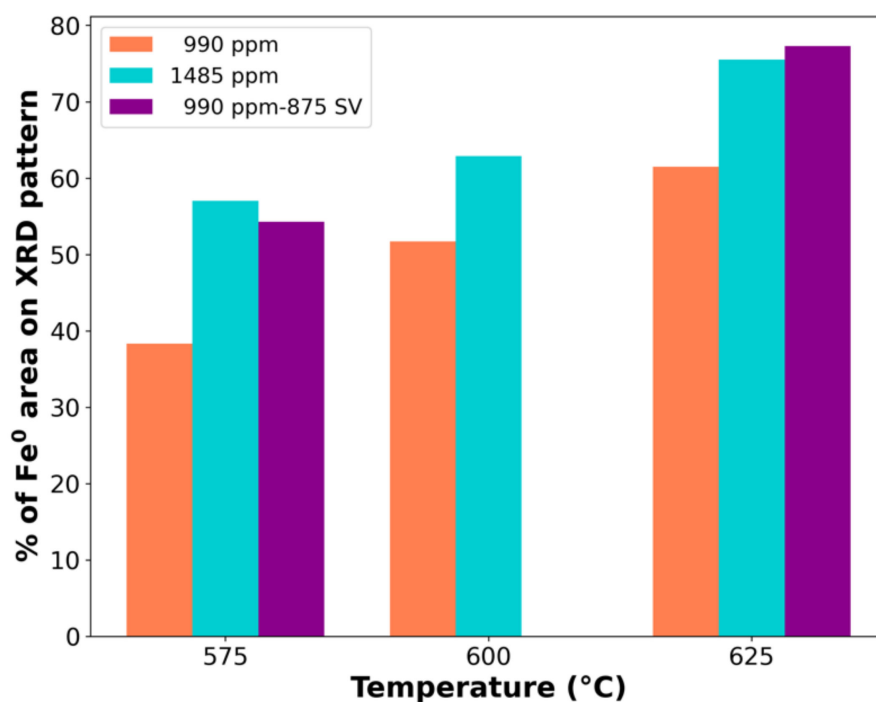

Figure 6. Percentage of Fe^0 remaining in the Fe/CAG spent catalyst at different conditions. Each experiment is denoted with the toluene concentration in the feed. All experiments were carried out at 700 mL/(min·g_{cat}), except for spent catalysts marked 875 SV, which were performed at 875 mL/(min·g_{cat}).

2.4.2. Reaction in Quasi-Real Conditions

Naphthalene is considered the most difficult tar constituent to be decomposed [46]. As was described before, the Fe/CAG-ps catalyst (used at bench-scale) has similar properties to the Pd/CAG, but is shaped as pellets to avoid a high pressure drop in the catalytic bed.

Figure 7 shows the behavior of experiments in dynamic conditions. These results evidenced a first period of stabilization where the conversion decreased at all reaction conditions. The total loss of activity registered for the steady state at 565 °C and 665 °C coincided with the extensive oxidation of Fe^0 and the absence of carbides, as confirmed by the XRD pattern, as is discussed below. Conversely, the presence of CO in the gas stream at the same temperatures led to an increase in naphthalene conversion, even when the CO promoted the oxidation of metal clusters. This apparent contradiction suggests that, in the presence of CO, the reaction mechanism changed or the carbothermic reduction of Fe_xO_y was promoted, generating additional active sites for naphthalene conversion.
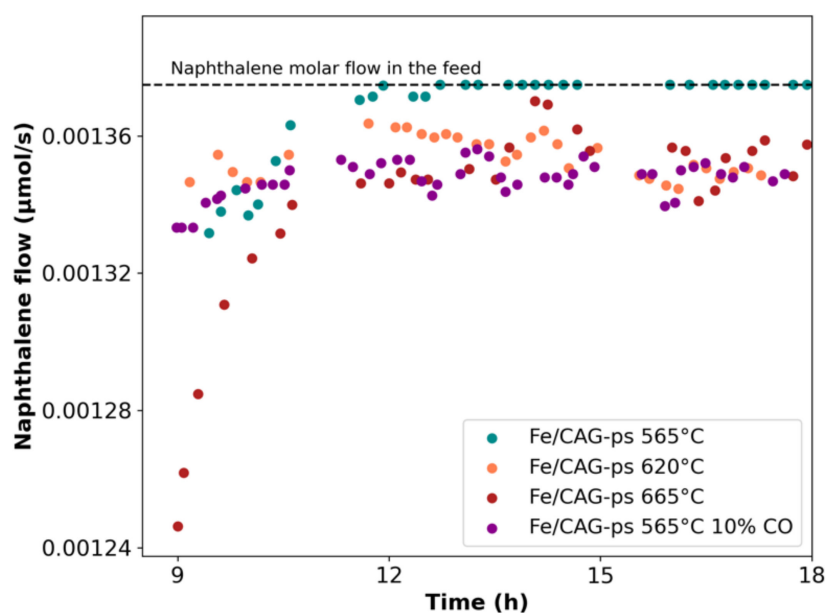
Figure 7. Naphthalene decomposition on Fe/CAG-ps at different temperatures and with co-fed CO at 565 °C; both 960 mL/(min·g_{cat}) space velocity, 3130 ppmv of benzene, 660 ppmv of naphthalene.

The experiments shown here suggest differences between reaction mechanisms for toluene and naphthalene decomposition. While the benzene produced after toluene decomposition is consumed completely in the reaction, suggesting the presence of free active sites, the benzene produced during naphthalene decomposition leaves the reactor. Naphthalene should be adsorbed on the surface by one ring in the planar form [38]. According to the results of the experiments with pure benzene in the feed, both catalysts are capable of breaking the aromatic ring, due to their similar characteristics. It is possible to assume that the ring from the naphthalene molecule in contact with the surface is broken, and the second ring is released, increasing benzene concentration in the product gas.

The kinetic measurements for naphthalene decomposition (without CO co-feed) over Fe/CAG-ps exhibit a similar behavior as for toluene (Figure 8), but in this case we attributed the slope change to the partial deactivation of the catalyst. According to Equation (11), a change in the balance of the most abundant reaction intermediate (MARI) by the catalyst deactivation (carbon deposited or change in the Fe^0/Fe^{+n} site balance) could imply a proportional effect in the Q_i (see Equation (12)). To confirm such deactivation, the spent catalysts were characterized by XRD and the activity measurements were discussed along with the nature of metal sites.
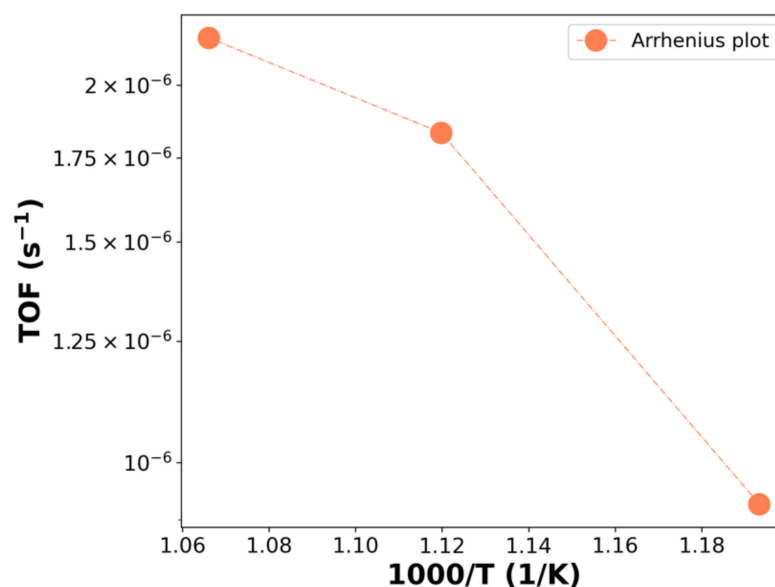
Figure 8. Arrhenius plot for naphthalene decomposition over Fe/CAG-ps. Temperature values: 565 °C, 620 °C, and 665 °C.

Oxide formation on metal clusters was verified by the XRD patterns for the spent catalysts (Figure 9 and Table A3). Again, the loss in activity for naphthalene conversion is attributed to the formation of Fe oxides of different nature [47]. The oxide formation depends on O availability; at higher O concentration, the oxidation state changes from FeO to Fe_3O_4 and finally to γ-Fe_2O_3 [48]. The catalysts used in experiments with CO in the feed showed a higher oxidation degree after being used. The CO favored the Fe oxidation, which is why the XRD patterns for those spent catalysts show almost exclusively γ-Fe_2O_3 and Fe_3C phases.
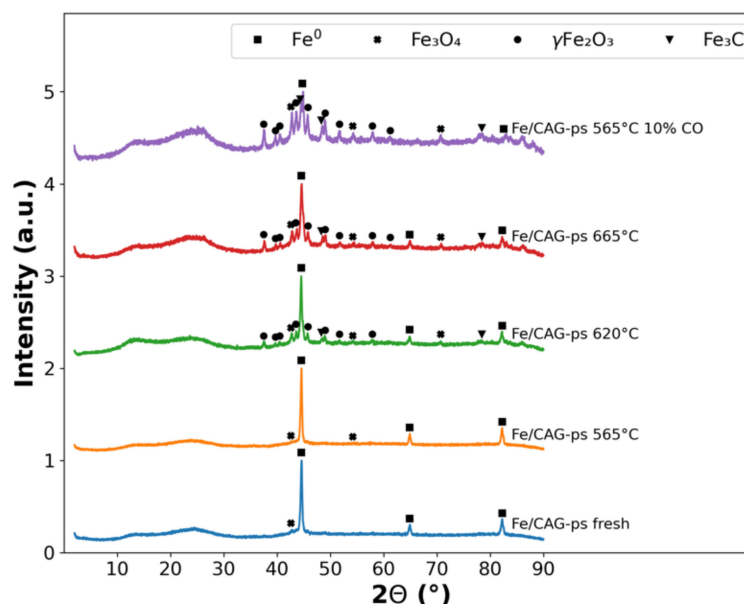
Figure 9. XRD pattern of fresh and spent Fe/CAG-ps during naphthalene decomposition.

3. Discussion

The performed experiments allow the proposal of a mechanism for the decomposition of different tar components. Benzene and toluene decomposition over Fe/CAG compared at similar conditions show strong differences; while benzene is consumed, toluene conversion is poor. The decomposition of each generates the other tar, suggesting that the elementary

step on the surface of the Fe/CAG that governs the conversion of toluene into benzene and vice versa, seems to be reversibly balanced. The model that is proposed with these results can explain the drop in the activity not related to Fe oxidation. According to the model's apparent activation energy expression, a decrease in toluene conversion can be caused by the concentration of surface intermediates decreasing at higher temperatures while the modular values of toluene adsorption and dissociation remain constant.

On the other hand, naphthalene decomposition over Fe/CAG-ps produces benzene as the main product, evidenced in a rise of benzene concentration fed together with naphthalene (Table A4). This suggests that the surface is covered by naphthalene, preventing benzene decomposition after its formation during the naphthalene break. The incorporation of CO into the reactor generates an increment in naphthalene conversion. However, CO promotes oxidation of the active phase at a level higher than observed during decomposition of pure tars where only the support contains O in the solid matrix. Contrary to what is expected, this oxidation does not deactivate the catalyst, due to the formation of Fe_3C, which probably acts as a new active site. The present work opens the discussion to the possibility that iron carbides act as active sites, which is of marked importance since this metal is one of the most abundant and environmentally friendly active phases available for gasification gas cleaning.

4. Materials and Methods

4.1. CAG Promotor Cellulose Microfibrils

The University of Maine (U.S.A.) provided the freeze-dried microfibrils used for the CAG preparation. The cellulose microfibrils (MFC) were prepared from a gel produced from a bleached Kraft pulp at 3% wt of solids. The gels were freeze-dried according to the procedure reported by Demers [49] and known as ice segregation induced self-assembling (ISISA). The MFC were treated with a flame retardant. The freeze-dried MFC, were disk-shaped (200 mg of MFC, 10 mm diameter, 2 mm of thickness) in a Parr press (Parr Instrument Company, Moline, IL, U.S.A.). The pellets were impregnated via incipient wetness with an appropriate amount of ammonium sulfate ((NH_4)$_2SO_4$, 99.5% purity, Merck, Darmstadt, germany) to achieve 5% wt (dry basis) of salt in the pellets, according to a procedure reported in [50]. Impregnated samples were dried at 40 °C for 20 h, and the impregnation effectivity was confirmed by gravimetric analysis.

4.2. CAG Preparation

Carbonization of the pre-treated MFC was carried out in a split Thermo Scientific Lindberg/Blue M tube furnace. Approximately 7.4 g of pre-treated MFC were pelletized in a manual press (Parr Instrument Company, Moline, IL, U.S.A.) prior to carbonization. Then, 36 pellets of 10 mm (DI), 2 mm of height were stacked in aluminum-oxide trays, which were placed in parallel to the direction of N_2 gas flow (Air Liquide, 99.999% purity, Coronel, Chile) of 20 mL/(min·g_{cat} of sample). The Thermo Scientific Lindberg/Blue M tube furnace was heated up to 900 °C at a constant heating rate of 10 °C/min, without dwell time. The resulting solid was a carbon aerogel (CAG) used as the catalyst support, and ground under 53 μm for lab scale experiments or kept as pellets of ~8 mm diameter × 1.5 mm high after carbonization. These conditions were optimized in a previous study [34].

4.3. Preparation of Catalysts

For toluene decomposition, catalysts with 10% wt of Fe were prepared via incipient wetness impregnation. Iron nitrate (Fe(NO_3)$_3$·9H_2O, >99% purity, Merck, Darmstadt, germany), was used as a metal precursor. Briefly, the corresponding salt aqueous solution was added dropwise to the CAG support (<80 meshes) in the appropriate quantity, to reach 10% wt of metal in the final catalyst, according to the pore volume determined by N_2 adsorption–desorption (see Section 4.5). For the bench-scale experiments, CAG pellets were impregnated to obtain the same metal loading (10% wt) without a previous grounding of the support. Thereafter, the metal-loaded samples were dried at 105 °C for 4 h and reduced

for 2 h at 700 °C, under 40 mL/min of H_2, using a heating rate of 2 °C/min to reach the final temperature before each tar decomposition experiment. Synthetized catalysts were identified as Fe/CAG and Fe/CAG-ps, where 'ps' refers to pellet shape.

Spent catalysts nomenclature was specified as *Catalyst Name–Temperature–Initial tar concentration_Space velocity* (only if space velocity was different to 700 mL/(min·g_{cat}). For example, a sample of Fe/CAG-ps used at 600 °C with an initial toluene concentration of 990 ppm under a space velocity of 875 mL/(min·g_{cat}) was denoted as Fe/CAG-ps 600-990 SV875.

4.4. Compositional Analysis

Inductively coupled plasma optical emission spectrometry (ICP-OES) analysis was performed to determine the actual content of metal on the catalysts Fe/CAG and Fe/CAG-ps. Support samples were also characterized using standard practice for elemental analysis [51] and a Leco TruSpec analyzer (LECO Argentina S.A., Buenos Aires, Argentina). The main and trace inorganic elements were quantified using a PerkinElmer Optima 7000 DV ICP-OES series instrument to discard the presence of other metals with reported catalytic activity in tar decomposition.

4.5. N_2-Physisorption

N_2 adsorption was performed to estimate the specific surface area using the Brunauer-Emmet–Teller (BET) model and pore volume. Barret–Joyner–Halenda (BJH) pore size distribution was determined using desorption data. Both isotherms were recorded in a Micromeritics Gemini VII 2390t device (Micromeritics, Communications Dr, Norcross, GA, USA), for support and catalysts. Before tests, 0.2–0.5 g of samples were degassed at 150 °C under a continuous pure N_2 flow for 24 h, as recommended by De Lange et al. [52].

4.6. X-ray Diffraction (XRD)

XRD analysis of catalysts before and after use was performed to evaluate the crystallite size of the samples and changes in oxidation states during the reaction. The XRD patterns were recorded on a Bruker AXS model D4 Endeavor diffractometer (Bruker AXS GmgH, Karsruhe, Germany), using monochromatic CuKα radiation (λ = 0.15418). The signal was generated at 40 kV and 20 mA. The intensities were measured in the range 5° < 2θ < 90° for CAGs, with a step size of 0.02° and scans at one s/step. The crystallite apparent size was calculated using Scherrer's equation for all solids (Equation (13)).

$$L = \frac{K\lambda}{\beta \cos(\theta)} \tag{13}$$

where K is a constant equal to 0.94 for all catalyst samples, λ is the wavelength (in nm), β is the full width at half-maximum intensity (FWHM) (in rad), and θ is the plane angle.

4.7. Transmission Electron Microscopy (TEM)

The metal particle sizes for the catalyst were measured from transmission electron microscopy images, recorded in a JEOL JEM 1200 EXII device (JEOL Ltd., Peabody, MA, USA), with voltage 120 kV. The sample was suspended in a solution of ethanol–water (50% wt), supported in a copper grill, and covered by a carbon layer. The size distribution and mean cluster sizes were estimated after measuring more than 10 images.

4.8. Scanning Electron Microscopy–Energy Dispersive X-ray Spectroscopy (SEM–EDX)

Carbon deposition on the Fe catalysts was correlated by comparing the C/Fe ratio before and after the reaction. The relative amounts of C, H, N, O, and Fe elements were estimated using SEM–EDX in a LEO 1420VP microscope using 300 × magnification for fresh and used (during toluene decomposition) Fe/CAG. Similar elements were recorded in a TESCAN VEGA3 SBU EasyProbe device for fresh and used (during naphthalene decomposition) Fe/CAG-ps. The change in the C/Fe ratio was attributable to the C

deposition or consumption during the reaction, assuming negligible or no Fe loss in the process.

4.9. Kinetic Measurements for Tars Decomposition on Fe/CAG

The activity tests were carried out in a custom-designed system (Figure 10) using 100 mg of Fe/CAG catalyst (fine powder, 53 μm < particle size < 73 μm), which was loaded into a U-shape quartz reactor (10 mm inside diameter) placed inside a tubular furnace (Omega Eng, CRFC-312/240-C-A, Stamford, CT, USA).
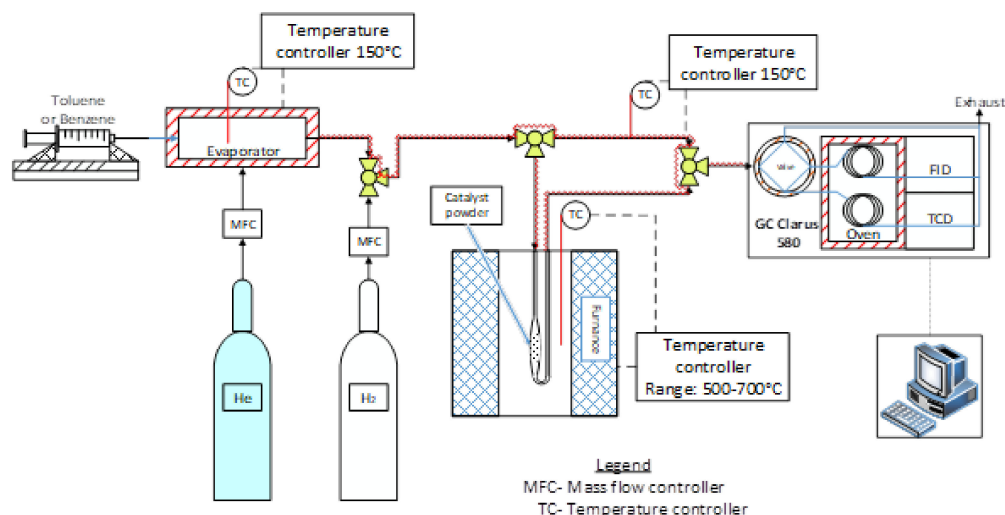
Figure 10. Representation of lab-scale workplace for tar decomposition.

The tar sample (toluene >99% purity, Merck, Darmstadt, Germany) was fed by a syringe pump (Cole–Parmer GmbH, Wertheim, Germany) to a custom-made evaporator where a He flow (Air Liquide, 99.999% purity, Coronel, Chile) circulated with a specific rate according to the required concentration between 900 and 1979 ppm of tar. A mass flow controller (Kofloc, model 8500, Kyoto, Japan) was used to control the He flow. Both He and toluene streams were oxygen-free. All pipes were heated at 150 °C using heating tapes (Omega Eng, Stamford, CT, U.S.A.), and a reactor by-pass was installed to measure the feed concentration before the reaction. The composition of reactant and product streams were analyzed in a Clarus 580 GC (Perkin Elmer, Santiago de Chile, Chile) equipped with an Elite-5 (PerkinElmer, Chile) and a Carboxen-1000 (Supelco Analytical, Darmstadt, Germany) column coupled to FID and TCD detectors, respectively.

The sample was injected by a 10-way automatic valve heated at 150 °C. The feed concentrations and reaction temperatures were varied to estimate the kinetic parameters. The reaction products, identified by comparing their ionization patterns were measured in a gas chromatograph (GC-2010 Plus, Shimadzu, Montevideo, Uruguay) equipped with a single quadrupole mass spectrometry detector (QP 2010 Ultra, Shimadzu, Montevideo, Uruguay) with the NIST database.

The conversion of toluene (x) was calculated according to Equation (14) assuming constant volume and pressure.

$$x = \frac{Pp^{\circ}_{Toluene} - Pp^{f}_{Toluene}}{Pp^{\circ}_{Toluene}} \tag{14}$$

where $Pp^{\circ}_{Toluene}$ and $Pp^{f}_{Toluene}$ are the partial pressure of toluene at the inlet and outlet of the reactor, respectively.

4.10. Evaluation of the Catalytic Performance of Fe/CAG-ps for a Tar Mixture

The effectivity of the Fe/CAG-ps catalysts for converting model tar was studied at the bench-scale plant installed in the Fraunhofer Institute for Environmental, Safety and Energy Technology (UMSICHT) facilities in Oberhausen, Germany. A detailed description of this system was reported in a previous paper and a schematization is provided in Figure 11 [53]. In a typical experiment, the reactor was loaded with 1 g of catalyst, using a small steel basket.
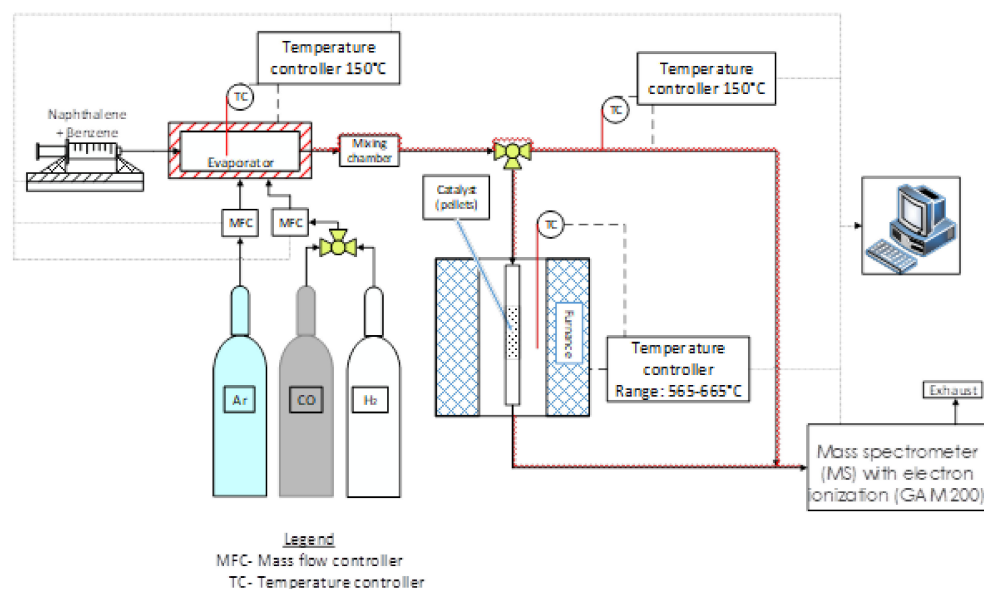
Figure 11. Representation of bench-scale workplace for tar decomposition.

The experiments (Table 2) were performed at a fixed ratio of 2.45:1 $(mL/min)_{bzn}/(mL/min)_{nph}$, except for 1 control experiment carried out under pure benzene at 565 °C. The CO and H2 (Linde gas, Munich, Germany) were fed along with the tar model mixture to emulate a real syngas [54–56]. Gas composition was measured before and after the reaction by switching the position of a multiport valve (Valco Instruments Co. Inc., Houston, TX, U.S.A.). The tar constituents studied here (benzene, toluene, and naphthalene, >99% purity, Merck, Darmstadt, Germany) did not suffer thermal decomposition (homogeneous reaction) in the temperature and residence time ranges studied here [8].

Table 2. Experiments carried out with benzene: naphthalene flowrate ratio of 2.45:1 (catalyst: 1 g, space velocity 940–960 mL/min g catalyst).

N°	Temperature (°C)	Gases [1] (*v/v*)
1	565	Ar (balance)
2	620	Ar (balance)
3	660	Ar (balance)
4	565	10% CO, Ar (balance)

[1] CO > 99.5% and Ar > 99.999%, Linde gas, Munich, Germany.

Author Contributions: O.G.-C., R.J.C. and L.E.A.-P. conceived and designed the experiments; O.G.-C. and K.M. performed the experiments; O.G.-C. analyzed and curated the data; O.G.-C. performed the writing—original draft preparation; L.E.A.-P., R.J.C. and T.S. performed the writing—review and editing; L.E.A.-P. and R.J.C. performed supervision and project administration. All authors have read and agreed to the published version of the manuscript.

Conflicts of Interest: The authors declare no conflict of interest.

Appendix A

Table A1. XRD planes identifications in spent Fe/CAG.

Signal's Angle (°)	Plane	Metal Phase	References
30	(220)	Fe_3O_4	[57,58]
35.4	(311)	FeO	[57,58]
43	(400)	Fe_3O_4	[57,58]
44.6	(110)	Fe^0	[59]
54	(422)	Fe_3O_4	[57,58]
56.9	(511)	Fe_3O_4	[57,58]
62.5	(440)	FeO	[57,58]
65	(220)	Fe^0	[59]
82.2	(211)	Fe^0	[59]

Table A2. Particle size, estimated and by XRD patterns, for three different Fe phases in toluene decomposition spent catalysts.

Catalysts	Particle Size (nm)			Pattern Area	
	FeO (311)	Fe^0 (110)	Fe_3O_4 (511)	Fe^0 (%)	Fe^{x+} (%)
Fe/CAG fresh	-	27.1	-	~99	~1
Fe/CAG 575 °C-990	19.7	31.7	15.2	38.3	61.7
Fe/CAG 600 °C-990	21.2	29.6	17.3	51.7	48.3
Fe/CAG 625 °C-990	17.4	30.2	14.9	61.5	38.5
Fe/CAG 575 °C-1485	20.0	29.6	16.4	57	43
Fe/CAG 600 °C-1485	18.7	29.6	17.3	62.9	37.1
Fe/CAG 625 °C-1485	17.0	29.3	20.0	75.5	24.5
Fe/CAG 575 °C-990 SV 875	21.9	30.8	14.8	54.3	45.7
Fe/CAG 625 °C-990 SV 875	20.5	30.8	14.3	77.3	22.7

Table A3. XRD plane identification in spent Fe/CAG-ps.

Signal's Angle (°)	Plane	Metal Phase	References
37.6	(222)	Fe_3O_4	[48]
39.7	(109)	γ-Fe_2O_3	[48]
40.6	(119)	γ-Fe_2O_3	[48]
43	(400)	Fe_3O_4	[57,58]
43.7	(202)	α-Fe_2O_3	[48]
44.56	(102)	Fe_3C	[60]
44.6	(110)	Fe^0	[59]
45.8	(330)	γ-Fe_2O_3	[48]
49.12	(112)	Fe_3C	[60]
50	(421)	γ-Fe_2O_3	[48]
51.7	(00 12)	γ-Fe_2O_3	[48]
54	(422)	Fe_3O_4	[57,58]
58	(21 12)	γ-Fe_2O_3	[48]
61.8	(440)	γ-Fe_2O_3	[57,58]
65	(220)	Fe^0	[59]
70.7	(620)	Fe_3O_4	[48]
78.6	(133)	Fe_3C	[60]
82.2	(211)	Fe^0	[59]

Table A4. Benzene flow in the exhaust at different temperatures and feed conditions.

Catalysts	Benzene Flow Inlet (μmol/s)	Benzene Flow Exhaust (μmol/s)	Change (%)
Fe/CAG-ps 565 °C	0.00424	0.004314	1.57
Fe/CAG-ps 620 °C	0.00424	0.004310	1.47
Fe/CAG-ps 665 °C	0.00424	0.004308	1.44
Fe/CAG-ps 565 °C 10% CO	0.00424	0.004296	1.15
Fe/CAG-ps 565 °C (pure benzene)	0.00424	0.00390	−8.01

References

1. Molino, A.; Larocca, V.; Chianese, S.; Musmarra, D. Biofuels production by biomass gasification: A review. *Energies* **2018**, *11*, 811. [CrossRef]
2. Rios, M.L.V.; González, A.M.; Lora, E.E.S.; del Olmo, O.A.A. Reduction of tar generated during biomass gasification: A review. *Biomass Bioenergy* **2018**, *108*, 345–370. [CrossRef]
3. Li, C.; Suzuki, K. Resources, properties and utilization of tar. *Resour. Conserv. Recycl.* **2010**, *54*, 905–915. [CrossRef]
4. Zwart, R.W.R. *Gas Cleaning Downstream Biomass Gasification Status Report 2009*; ECN SenterNovem: Petten, The Netherlands, 2009.
5. You, S.; Ok, Y.S.; Tsang, D.C.W.; Kwon, E.E.; Wang, C.H. Towards practical application of gasification: A critical review from syngas and biochar perspectives. *Crit. Rev. Environ. Sci. Technol.* **2018**, *48*, 1165–1213. [CrossRef]
6. Arregi, A.; Amutio, M.; Lopez, G.; Bilbao, J.; Olazar, M. Evaluation of thermochemical routes for hydrogen production from biomass: A review. *Energy Convers. Manag.* **2018**, *165*, 696–719. [CrossRef]
7. Hu, J.; Li, D.; Lee, D.J.; Zhang, Q. Gasification and catalytic reforming of corn straw in closed-loop reactor. *Bioresour. Technol.* **2019**, *282*, 530–533. [CrossRef]
8. Jess, A. Mechanisms and kinetics of thermal reactions of aromatic hydrocarbons from Pyrolysis of Solid Fuels. *Fuel* **1996**, *75*, 1441–1448. [CrossRef]
9. Gai, C.; Dong, Y.; Fan, P.; Zhang, Z.; Liang, J.; Xu, P. Kinetic study on thermal decomposition of toluene in a micro fluidized bed reactor. *Energy Convers. Manag.* **2015**, *106*, 721–727. [CrossRef]
10. Zhou, Y.; Wang, W.; Sun, J.; Song, Z.; Zhao, X.; Mao, Y. Decomposition of methylbenzene over Fe0/ZSM-5 under microwave irradiation. *Catal. Commun.* **2017**, *96*, 63–68. [CrossRef]
11. Zhang, Y. In-situ IR study for elucidating the adsorption cracking mechanism of toluene over calcined olivine catalyst. *Int. J. Hydrogen Energy* **2018**, *43*, 15835–15842. [CrossRef]
12. Janajreh, I.; Adeyemi, I.; Raza, S.S.; Ghenai, C. A review of recent developments and future prospects in gasification systems and their modeling. *Renew. Sustain. Energy Rev.* **2021**, *138*, 110505. [CrossRef]
13. Ramadhani, B.; Kivevele, T.; Kihedu, J.H.; Jande, Y.A.C. Catalytic tar conversion and the prospective use of iron-based catalyst in the future development of biomass gasification: A review. *Biomass Convers. Biorefin.* **2020**, *12*, 1369–1392. [CrossRef]
14. Rapagnà, S.; Jand, N.; Kiennemann, A.; Foscolo, P.U. Steam-gasification of biomass in a fluidised-bed of olivine particles. *Biomass Bioenergy* **2000**, *19*, 187–197. [CrossRef]
15. Abu El-Rub, Z.; Bramer, E.A.; Brem, G. Review of Catalysts for Tar Elimination in Biomass Gasification Processes. *Ind. Eng. Chem. Res.* **2004**, *43*, 6911–6919. [CrossRef]
16. Dos Santos, R.G.; Alencar, A.C. Biomass-derived syngas production via gasification process and its catalytic conversion into fuels by Fischer Tropsch synthesis: A review. *Int. J. Hydrogen Energy* **2020**, *45*, 18114–18132. [CrossRef]
17. Wang, L.; Li, D.; Koike, M.; Koso, S.; Nakagawa, Y.; Xu, Y.; Tomishige, K. Catalytic performance and characterization of Ni-Fe catalysts for the steam reforming of tar from biomass pyrolysis to synthesis gas. *Appl. Catal. A Gen.* **2011**, *392*, 248–255. [CrossRef]
18. Min, Z.; Yimsiri, P.; Asadullah, M.; Zhang, S.; Li, C.-Z. Catalytic reforming of tar during gasification. Part II. Char as a catalyst or as a catalyst support for tar reforming. *Fuel* **2011**, *90*, 2545–2552. [CrossRef]
19. Zhang, J.; Jiang, P.; Gao, F.; Ren, Z.; Li, R.; Chen, H.; Ma, X.; Hao, Q. Fuel gas production and char upgrading by catalytic CO_2 gasification of pine sawdust char. *Fuel* **2020**, *280*, 118686. [CrossRef]
20. Xu, R.; Kong, X.; Zhang, H.; Ruya, P.M.; Li, X. Destruction of gasification tar over Ni catalysts in a modified rotating gliding arc plasma reactor: Effect of catalyst position and nickel loading. *Fuel* **2021**, *289*, 119742. [CrossRef]
21. Huber, G.W.; Iborra, S.; Corma, A. Synthesis of transportation fuels from biomass: Chemistry, catalysts, and engineering. *Chem. Rev.* **2006**, *106*, 4044–4098. [CrossRef]
22. Stevens, D.J. *Hot Gas Conditioning: Recent Progress with Larger-Scale Biomass Gasification Systems*; OSTI: Washingtion, DC, USA, 2001.
23. Virginie, M.; Courson, C.; Niznansky, D.; Chaoui, N.; Kiennemann, A. Characterization and reactivity in toluene reforming of a Fe/olivine catalyst designed for gas cleanup in biomass gasification. *Appl. Catal. B Environ.* **2010**, *101*, 90–100. [CrossRef]
24. Claude, V.; Mahy, J.G.; Douven, S.; Pirard, S.L.; Courson, C.; Lambert, S.D. Ni- and Fe-doped γ-Al2O3 or olivine as primary catalyst for toluene reforming. *Mater. Today Chem.* **2019**, *14*, 100197. [CrossRef]
25. Li, X.; Wang, L.; Zhang, B.; Khajeh, A.; Shahbazi, A. Iron oxide supported on silicalite-1 as a multifunctional material for biomass chemical looping gasification and syngas upgrading. *Chem. Eng. J.* **2020**, *401*, 125943. [CrossRef]

26. Madadkhani, S.; Burhenne, L.; Bi, X.; Ellis, N.; Grace, J.R.; Lewis, T. Bauxite residue as an iron-based catalyst for catalytic cracking of naphthalene, a model compound for gasification tar. *Can. J. Chem. Eng.* **2021**, *99*, 1461–1474. [CrossRef]

27. Duvenhage, D.J.; Espinoza, R.L.; Coville, N.J. Fischer-Tropsch precipitated iron catalysts: Deactivation studies. *Stud. Surf. Sci. Catal.* **1994**, *88*, 351–358. [CrossRef]

28. Zhang, Y.; Kajitani, S.; Ashizawa, M.; Oki, Y. Tar destruction and coke formation during rapid pyrolysis and gasification of biomass in a drop-tube furnace. *Fuel* **2010**, *89*, 302–309. [CrossRef]

29. Bhandari, P.N.; Kumar, A.; Huhnke, R.L. Simultaneous Removal of Toluene (Model Tar), NH_3, and H_2S, from Biomass-Generated Producer Gas Using Biochar-Based and Mixed-Metal Oxide Catalysts. *Energy Fuels* **2013**, *28*, 1918–1925. [CrossRef]

30. Korus, A.; Samson, A.; Szle, A.; Katelbach-woz, A.; Sladek, S. Pyrolytic toluene conversion to benzene and coke over activated carbon in a fixed-bed reactor. *Fuel* **2017**, *207*, 283–292. [CrossRef]

31. Fuentes-Cano, D.; Gómez-Barea, A.; Nilsson, S.; Ollero, P. Decomposition kinetics of model tar compounds over chars with different internal structure to model hot tar removal in biomass gasification. *Chem. Eng. J.* **2013**, *228*, 1223–1233. [CrossRef]

32. Meng, Y.; Young, T.M.; Liu, P.; Contescu, C.I.; Huang, B.; Wang, S. Ultralight carbon aerogel from nanocellulose as a highly selective oil absorption material. *Cellulose* **2014**, *22*, 435–447. [CrossRef]

33. Ábrahám, D.; Nagy, B.; Dobos, G.; Madarász, J.; Onyestyák, G.; Trenikhin, M.V.; László, K. Hydroconversion of acetic acid over carbon aerogel supported molybdenum catalyst. *Microporous Mesoporous Mater.* **2014**, *190*, 46–53. [CrossRef]

34. Perez, L.E.A.; Gómez-Cápiro, O.; Hinkle, A.; Delgado, A.M.; Fernández, C.; Jiménez, R.; Arteaga-Pérez, L.E. Carbon Aerogel-Supported Nickel and Iron for Gasification Gas Cleaning. Part I: Ammonia Adsorption. *Catalysts* **2018**, *8*, 347. [CrossRef]

35. Arteaga-Pérez, L.E.; Gómez Cápiro, O.; Romero, R.; Delgado, A.; Olivera, P.; Ronsse, F.; Jimenez, R. In situ catalytic fast pyrolysis of crude and torrefied Eucalyptus globulus using carbon aerogel-supported catalysts. *Energy* **2017**, *128*, 701–712. [CrossRef]

36. Arteaga-Pérez, L.E.; Jiménez, R.; Grob, N.; Gómez, O.; Romero, R.; Ronsse, F. Catalytic upgrading of biomass-derived vapors on carbon aerogel-supported Ni: Effect of temperature, metal cluster size and catalyst-to-biomass ratio. *Fuel Process. Technol.* **2018**, *178*, 251–261. [CrossRef]

37. Faúndez, J.M.; García, X.A.; Gordon, A.L. Kinetic approach to catalytic pyrolysis of tars. *Fuel Process. Technol.* **2001**, *69*, 239–256. [CrossRef]

38. Mukai, D.; Murai, Y.; Higo, T.; Tochiya, S.; Hashimoto, T.; Sugiura, Y.; Sekine, Y. In situ IR study for elucidating reaction mechanism of toluene steam reforming over Ni/La0.7Sr0.3AlO3-δcatalyst. *Appl. Catal. A Gen.* **2013**, *466*, 190–197. [CrossRef]

39. Kaisalo, N.; Simell, P.A.; Lehtonen, J. Benzene steam reforming kinetics in biomass gasification gas cleaning. *Fuel* **2016**, *182*, 696–703. [CrossRef]

40. Braida, W.J.; Pignatello, J.J.; Lu, Y.; Ravikovitch, P.I.; Neimark, A.V.; Xing, B. Sorption Hysteresis of Benzene in Charcoal Particles. *Environ. Sci. Technol.* **2003**, *37*, 409–417. [CrossRef]

41. Thommes, M.; Kaneko, K.; Neimark, A.V.; Olivier, J.P.; Rodriguez-Reinoso, F.; Rouquerol, J.; Sing, K.S.W. Physisorption of gases, with special reference to the evaluation of surface area and pore size distribution (IUPAC Technical Report). *Pure Appl. Chem.* **2015**, *87*, 1051–1069. [CrossRef]

42. Watwe, R.M.; Cortright, R.D.; Nørskov, J.K.; Dumesic, J.A. Theoretical Studies of Stability and Reactivity of C_2 Hydrocarbon Species on Pt Clusters, Pt(111), and Pt(211). *J. Phys. Chem. B* **2000**, *104*, 2299–2310. [CrossRef]

43. Van Santen, R.A. Complementary structure sensitive and insensitive catalytic relationships. *Acc. Chem. Res.* **2009**, *42*, 57–66. [CrossRef]

44. Fogler, H.S. *Elementos de Ingeniería de las Reacciones Químicas*, 4th ed.; Prentice Hall: Hoboken, NJ, USA, 2008; ISBN 9789702611981.

45. Oemar, U.; Ming Li, A.; Hidajat, K.; Kawi, S. Mechanism and kinetic modeling for steam reforming of toluene on $La_{0.8}Sr_{0.2}Ni_{0.8}Fe_{0.2}O_3$ catalyst. *AIChE J.* **2014**, *60*, 4190–4198. [CrossRef]

46. Devi, L.; Ptasinski, K.J.; Janssen, F.J.J.G. Decomposition of naphthalene as a biomass tar over pretreated olivine: Effect of gas composition, kinetic approach, and reaction scheme. *Ind. Eng. Chem. Res.* **2005**, *44*, 9096–9104. [CrossRef]

47. Duman, G.; Uddin, M.A.; Yanik, J. Hydrogen production from algal biomass via steam gasification. *Bioresour. Technol.* **2014**, *166*, 24–30. [CrossRef]

48. Kazeminezhad, I.; Mosivand, S. Phase transition of electrooxidized Fe_3O_4 to γ and α-Fe_2O_3 nanoparticles using sintering treatment. *Acta Phys. Pol. A* **2014**, *125*, 1210–1214. [CrossRef]

49. Spender, J.; Demers, A.L.; Xie, X.; Cline, A.E.; Earle, M.A.; Ellis, L.D.; Neivandt, D.J. Method for production of polymer and carbon nanofibers from water-soluble polymers. *Nano Lett.* **2012**, *12*, 3857–3860. [CrossRef]

50. Arteaga-Pérez, L.E.; Gómez-Cápiro, O.; Delgado, A.M.; Martín, S.A.; Jiménez, R. Elucidating the role of ammonia-based salts on the preparation of cellulose-derived carbon aerogels. *Chem. Eng. Sci.* **2017**, *161*, 80–91. [CrossRef]

51. *ABNT 8112*; Carvão Vegetal-Análise Imediata. Associação Brasileira de Normas: Rio de Janeiro, Brazil, 1968.

52. De Lange, M.F.; Vlugt, T.J.H.; Gascon, J.; Kapteijn, F. Adsorptive characterization of porous solids: Error analysis guides the way. *Microporous Mesoporous Mater.* **2014**, *200*, 199–215. [CrossRef]

53. Arteaga-Pérez, L.E.; Delgado, A.M.; Flores, M.; Olivera, P.; Matschuk, K.; Hamel, C.; Schulzke, T.; Jiménez, R. Catalytic conversion of model tars over carbon-supported Ni and Fe. *Catalysts* **2018**, *8*, 119. [CrossRef]

54. Lv, P.; Yuan, Z.; Ma, L.; Wu, C.; Chen, Y.; Zhu, J. Hydrogen-rich gas production from biomass air and oxygen/steam gasification in a downdraft gasifier. *Renew. Energy* **2007**, *32*, 2173–2185. [CrossRef]

55. Burhenne, L.; Rochlitz, L.; Lintner, C.; Aicher, T. Technical demonstration of the novel Fraunhofer ISE biomass gasification process for the production of a tar-free synthesis gas. *Fuel Process. Technol.* **2013**, *106*, 751–760. [CrossRef]

56. Sikarwar, V.S.; Zhao, M.; Fennell, P.S.; Shah, N.; Anthony, E.J. Progress in biofuel production from gasification. *Prog. Energy Combust. Sci.* **2017**, *61*, 189–248. [CrossRef]

57. Cheng, W.; Tang, K.; Qi, Y.; Sheng, J.; Liu, Z. One-step synthesis of superparamagnetic monodisperse porous Fe_3O_4 hollow and core-shell spheres. *J. Mater. Chem.* **2010**, *20*, 1799–1805. [CrossRef]

58. Shen, Y.; Zhao, P.; Shao, Q.; Ma, D.; Takahashi, F.; Yoshikawa, K. In-situ catalytic conversion of tar using rice husk char-supported nickel-iron catalysts for biomass pyrolysis/gasification. *Appl. Catal. B Environ.* **2014**, *152–153*, 140–151. [CrossRef]

59. Lin, W.S.; Lin, H.M.; Chen, H.H.; Hwu, Y.K.; Chiou, Y.J. Shape effects of iron nanowires on hyperthermia treatment. *J. Nanomater.* **2013**, *2013*, 237439. [CrossRef]

60. Yan, Q.; Wan, C.; Liu, J.; Gao, J.; Yu, F.; Zhang, J.; Cai, Z. Iron nanoparticles in situ encapsulated in biochar-based carbon as an effective catalyst for the conversion of biomass-derived syngas to liquid hydrocarbons. *Green Chem.* **2013**, *15*, 1631–1640. [CrossRef]